MDPI

Article

Corrosion Resistance and Nano-Mechanical Properties of a Superhydrophobic Surface

Chun-Wei Yao [1],*, Ian Lian [2], Jiang Zhou [1], Paul Bernazzani [3], Mien Jao [4] and Md Ashraful Hoque [1]

[1] Department of Mechanical Engineering, Lamar University, Beaumont, TX 77710, USA; zhoujx@lamar.edu (J.Z.); mhoque4@lamar.edu (M.A.H.)
[2] Department of Biology, Lamar University, Beaumont, TX 77710, USA; ilian@lamar.edu
[3] Department of Chemistry and Biochemistry, Lamar University, Beaumont, TX 77710, USA; pbernazzan@lamar.edu
[4] Department of Civil and Environmental Engineering, Lamar University, Beaumont, TX 77710, USA; jaomu@lamar.edu
* Correspondence: cyao@lamar.edu; Tel.: +1-409-880-7008

Abstract: Nanoindentation has been used to characterize the mechanical and creep properties of various materials. However, research on the viscoelastic and creep properties of superhydrophobic surfaces remains limited. In this study, a superhydrophobic coating was developed and its corrosion resistance was evaluated initially. Electrochemical impedance spectroscopy (EIS) results quantitatively confirm the enhanced anti-corrosion performance of the superhydrophobic coating. Subsequently, this study investigates the creep, hardness, strain rate sensitivity, and viscoelastic behavior of the superhydrophobic surface at the nanoscale before and after accelerated corrosion exposure. Our findings reveal that during the creep tests, the logarithmic values of creep strain rate and stress exhibited a good linear relationship. Additionally, the surface retains its key viscoelastic properties (hardness, storage modulus, loss modulus, and tan δ) even after exposure to corrosion. These results highlight the surface's robustness under corrosive conditions, a crucial factor for applications requiring both mechanical integrity and environmental resilience.

Keywords: corrosion resistance; nanoscale dynamic mechanical analysis; creep; superhydrophobic coating

1. Introduction

Superhydrophobic coatings possess significant properties, including anti-biofouling [1], self-cleaning [2], and anti-icing capabilities [3], and have introduced novel approaches for corrosion mitigation [4]. A key characteristic of superhydrophobic coating is the creation of unique hierarchical micro/nanostructures on substrates, which can trap significant amounts of air in an atmospheric environment, substantially reducing the contact area between water droplets and the surface [5–8]. To develop such coatings, two major requirements must be met: high surface roughness, which can be achieved by altering the surface topography at the micro/nanoscale [9], and low surface free energy, which can be achieved by modifying the surface chemistry [10]. Various methods can be employed to fabricate superhydrophobic coating, including nanocomposite coatings [11–14], chemical vapor deposition [15], self-assembled monolayers [16], and template methods [17]. These fabrication processes ensure that both surface roughness and low surface free energy are achieved to fulfill the essential requirements for superhydrophobic coatings.

Recent studies have employed nanoindentation to characterize the mechanical or creep properties of various materials. For example, studies have utilized nanoindentation

tests with different indentation loads to evaluate mechanical parameters or creep behavior, providing insights into the effects of load and loading strain rate on these properties [18–22]. Additionally, research on the nanoindentation creep behavior of nanocrystalline materials such as Ni, Ni-Fe alloys, and supercrystalline nanocomposites has revealed underlying mechanisms and apparent activation volumes [23,24]. Furthermore, nanoindentation has been extensively used to study the creep–fatigue interaction and local creep behavior of materials like P92 steel welded joints, offering valuable insights into the mechanical properties and creep deformation at the micro/nanoscale [25]. These studies underscore the importance of nanoindentation in understanding the nano-mechanical properties and creep behavior of various materials. Dynamic mechanical analysis (DMA) is crucial for measuring properties such as storage modulus, loss modulus, and damping capability (tan δ). This technique involves applying a sinusoidal stress to a material and measuring the resulting strain to determine its modulus. DMA is widely used to characterize a material's mechanical responses by tracking changes in its dynamic properties as a function of frequency, temperature, or time. Many researchers have utilized DMA as a supplementary test to evaluate the viscoelastic properties of nanomaterials used in micro/nano structured surface fabrication, alongside their tribological performance. More recently, researchers have conducted nano dynamic mechanical analysis (nano-DMA), where a sinusoidal stress is applied via a nanoindenter to characterize the viscoelastic properties of materials, such as storage modulus, loss modulus, and tangent delta [26–28]. These advanced techniques collectively contribute to a comprehensive understanding of material behavior at the nanoscale. However, reports on the nano-mechanical properties and creep behavior of superhydrophobic coatings are rarely seen. Typically, the performance of superhydrophobic coatings as corrosion inhibitors is evaluated by examining the corrosion behavior at the macroscale, often utilizing techniques like electrochemical impedance spectroscopy (EIS). Therefore, in this study, electrochemical impedance spectroscopy (EIS) was initially conducted on both steel and superhydrophobic coated substrates to understand their macroscale corrosion behavior. Subsequently, the nanohardness, strain rate sensitivity, and creep behavior of a superhydrophobic coating at the nanoscale were investigated before and after accelerated corrosion exposure. To the authors' knowledge, this study is the first to report the viscoelastic properties, including hardness, storage modulus, loss modulus, and tan δ, of a superhydrophobic surface, even after exposure to accelerated corrosion, at the nanoscale. The results provide crucial insights for the applications of the superhydrophobic coating, highlighting its potential for various industrial and engineering applications.

2. Materials and Methods

In this study, A653 steel substrates were used. The chemicals involved included acetone (Sigma Aldrich, St. Louis, MO, USA), isopropyl alcohol (Sigma Aldrich, St. Louis, MO, USA), anhydrous ethanol (Sigma Aldrich, St. Louis, MO, USA), and silane-modified hydrophobic SiO_2 nanoparticles (RX-50) with an average diameter of 55 ± 15 nm (Evonik, Piscataway, NJ, USA). Additionally, the polydimethylsiloxane (PDMS) elastomer kit (Sylgard 184) from Dow Corning was utilized.

The A653 steel substrates were degreased and cleaned ultrasonically for 20 min at room temperature. After cleaning, the substrates were rinsed thoroughly with isopropyl alcohol, ethanol, and deionized water [29]. To prepare the superhydrophobic surface solution, 1.7 g of PDMS and 11 g of toluene were combined and mixed in an ultrasonic mixer for 1 min to ensure proper dispersion. In a separate step, 2 g of silica nanoparticles was mixed with 10 g of toluene for 30 s in a planetary centrifugal mixer. The two solutions were then combined and mixed for an additional 30 s. Following this, 0.17 g of curing agent was added to the mixture, which was mixed again for 30 s in the centrifugal mixer,

followed by a 30 s defoaming process. The coating was applied using a spray gun at 80 MPa and room temperature, with the nozzle positioned 10 cm from the substrate and moved horizontally across the surface. Finally, the coated substrates were cured at ambient temperature (25 °C) in a fume hood for 3 days.

A drop shape analyzer (DSA25E, Krüss, Matthews, NC, USA) was employed to measure the static contact angle using 10 µL deionized water droplets at ambient temperature, as shown in Figure 1. The surface morphology of the superhydrophobic coated steel (SCS) substrate was evaluated using an atomic force microscope (AFM, Park NX10, Park System Co., Santa Clara, CA, USA), as shown in Figure 2a, and a scanning electron microscope (SEM, JSM-7500F, JEOL, Peabody, MA, USA), as shown in Figure 2b. An accelerated corrosion test was performed with a potentiostat system (Autolab PGSTAT204, Metrohm, Riverview, FL, USA) in a 3.5 wt.% NaCl solution at 0.135 V vs. open circuit potential for 90 min. A silver/silver chloride (Ag/AgCl) electrode served as the reference electrode, while a platinum wire mesh and the test specimen functioned as the counter electrode and working electrode, respectively. EIS measurements were conducted in a 3.5 wt% NaCl solution, with frequencies spanning from 0.01 Hz to 100 kHz and a wave amplitude of 10 mV, at room temperature. Nanoindentation tests and nano dynamic mechanical analysis were performed using a TI 980 TriboIndenter (Bruker, Eden Prarie, MN, USA) equipped with a three-sided Berkovich diamond tip before and after 90 min of accelerated corrosion. All creep and nano-DMA tests were conducted at a maximum nanoindentation force of 1000 µN at an ambient temperature of 25 °C. The thickness of the superhydrophobic surface was measured to be 35 µm using a digital coating thickness meter (Elcometer). At least three tests were performed for each measurement.
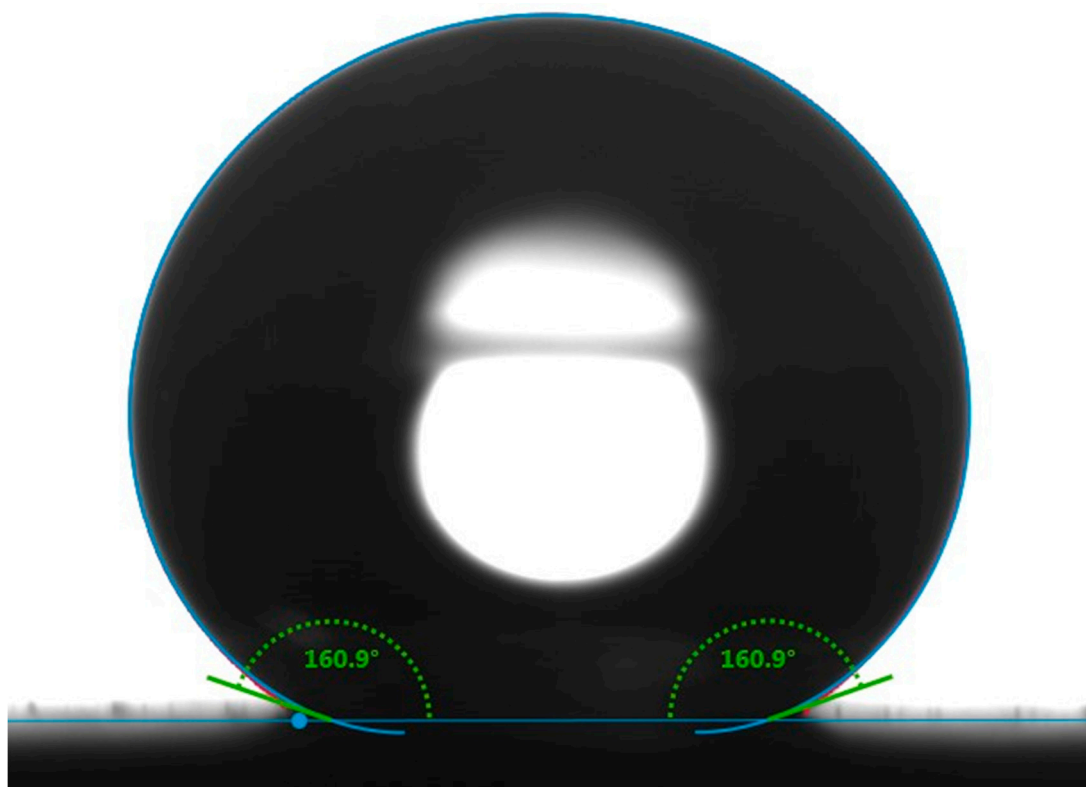

Figure 1. Static contact angle image for a water droplet of 10 µL on the superhydrophobic surface.
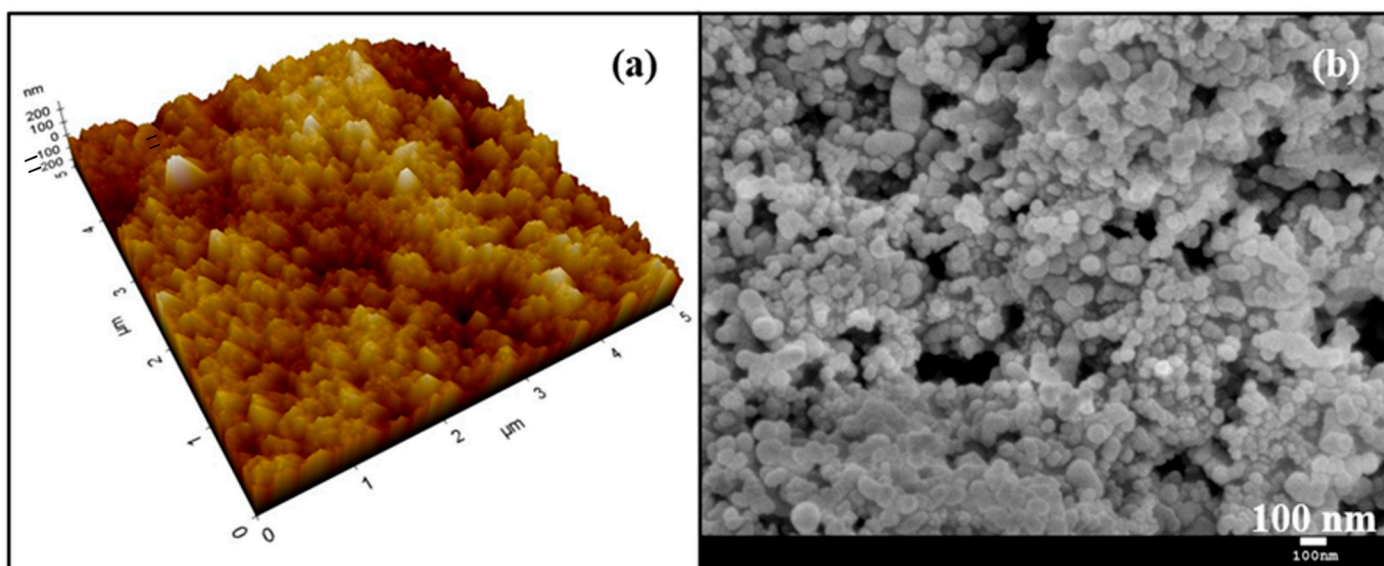
Figure 2. (**a**) Three-dimensional AFM image of the superhydrophobic surface; (**b**) SEM image of the superhydrophobic surface.

3. Results and Discussions

Figure 1 shows the static contact angle of the SCS sample. The incorporation of silica nanoparticles with PDMS resulted in a high static contact angle of 160.9°, indicative of the material's hydrophobic nature. The static contact angle was measured at five random locations, confirming the uniformity of the coating. Figure 2a shows the three-dimensional AFM image of the SCS sample. The microscale roughness, caused by the aggregation of nanoparticles, along with the nanoscale roughness from individual nanoparticles, created a hierarchical structure that enhanced the hydrophobicity of the SCS sample. Meanwhile, Figure 2b shows scanning electron microscopy (SEM) images of the SCS sample, where the dispersed nanoparticles within the network structure are clearly visible, further demonstrating the sample's textured surface.

The corrosion resistance of superhydrophobic-coated steel substrates was examined through electrochemical impedance spectroscopy (EIS) [13]. Figure 3a,b illustrate the equivalent circuit models for the steel and superhydrophobic coated substrates, respectively. The circuit elements in Figure 3a used to model the behavior of various interfaces and media in the system are defined as follows: Rs denotes the resistance of the electrolyte solution, and Rtop represents the resistance of the top steel surface. Qtop is the constant phase element associated with the top steel surface–electrolyte interface. Rd denotes the resistance of the diffusion layer over the top steel surface due to electrochemical reactions, while Qd represents the constant phase element for the diffusion layer at this interface. The Warburg impedance element (W) models the diffusional impedance for an infinitely thick diffusion layer. Figure 3b shows the equivalent electrical circuit used to simulate the case of the superhydrophobic coated substrate. In addition to Rs and W, the case introduces an additional resistance, Rscs, which represents the resistance attributed to the superhydrophobic coating, and Qscs, the constant phase element associated with the coating, based on its dielectric properties. Additionally, two more elements, Rd_scs and Qd_scs, represent the charge transfer resistance and constant phase element related to the diffusion layer at the interface. These elements are included to account for the distinct chemical interactions between the corrosive solution and the superhydrophobic coated substrate as compared to the steel substrate.
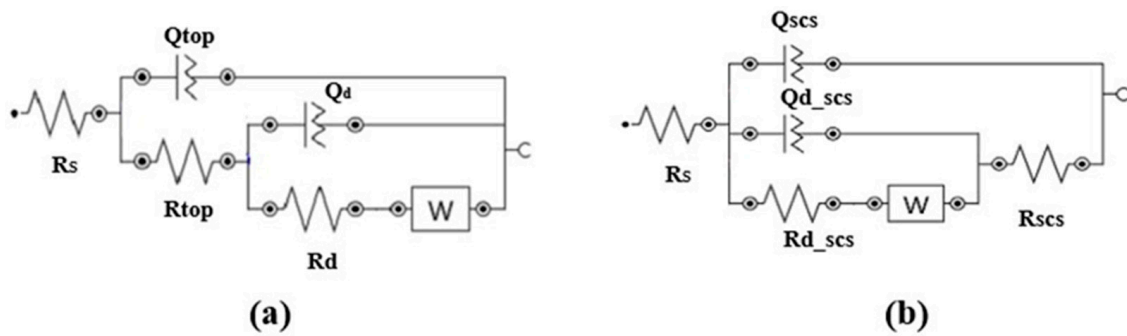
Figure 3. Electrical equivalent circuits for EIS of (**a**) steel substrate and (**b**) the superhydrophobic coated substrate.

Figure 4a presents the Nyquist plot, illustrating the relationship between the imaginary component of impedance ($-Z''$) and the real component (Z') for both substrate types. This plot shows a small semicircle for the steel substrate, corresponding to the diffusion layer resistance at the top surface–electrolyte interface, with an approximate diameter of 700 $\Omega \cdot$cm^2. For the superhydrophobic coated substrate, the semicircle diameter is notably larger, at 2.29 k$\Omega \cdot$cm^2, indicating a higher resistance of the diffusion layer and suggesting superior corrosion resistance for the coated substrate. Figure 4b provides the Bode plot of the impedance modulus ($|Z|$) as a function of log frequency for both substrates. At 1 MHz, the maximum applied frequency, the steel substrate exhibits an AC impedance modulus of 4.71 $\Omega \cdot$cm^2, while the superhydrophobic coated substrate achieves a significantly greater modulus of 700.55 $\Omega \cdot$cm^2. This elevated impedance at high frequency further reflects the resistive properties of the superhydrophobic coating, underscoring its enhanced corrosion resistance. The Bode plot of the phase angle (Φ) variation with frequency is displayed in Figure 4c. Here, the steel substrate shows a phase angle of 68.42°, whereas the superhydrophobic coating exhibits a reduced negative phase angle of 23.32°. The phase angle (Φ) can be determined by the following equation:

$$\Phi = \arctan\left(\frac{|Z_{Imaginary}|}{|Z_{Real}|}\right) \tag{1}$$

As Z_{Real} increases, the semicircle diameter also expands, signifying a high-resistance diffusion layer over the coated substrate. Hence, the decrease in phase angle further supports the improved corrosion resistance of the coated substrate. In addition, a strong agreement between experimental data and model fitting is observed as shown in Figure 4, suggesting that the equivalent circuit models fit very well with the experimental data. As one of the features of the superhydrophobic surface, air is trapped within the nanostructured morphology, which likely hinders the electrolyte solution from penetrating the surface structures and creates a high-resistance diffusion layer over the coated substrate.

Figure 5a shows the evolution of the creep displacement with a creep time of 600 s with the SCS sample before corrosion occurred and after 90 min of accelerated corrosion. The SCS sample's creep behaviors did not show any significant difference even after 90 min of accelerated corrosion. Both creep−time curves show a two-stage upward trend: an initial rapid rise within the first ∼50 s, which corresponds to the instable primary creep, followed by a slow linear increase, which corresponds to a more stable secondary creep. Therefore, it indicated that SCS possesses viscoelasticity at room temperature.
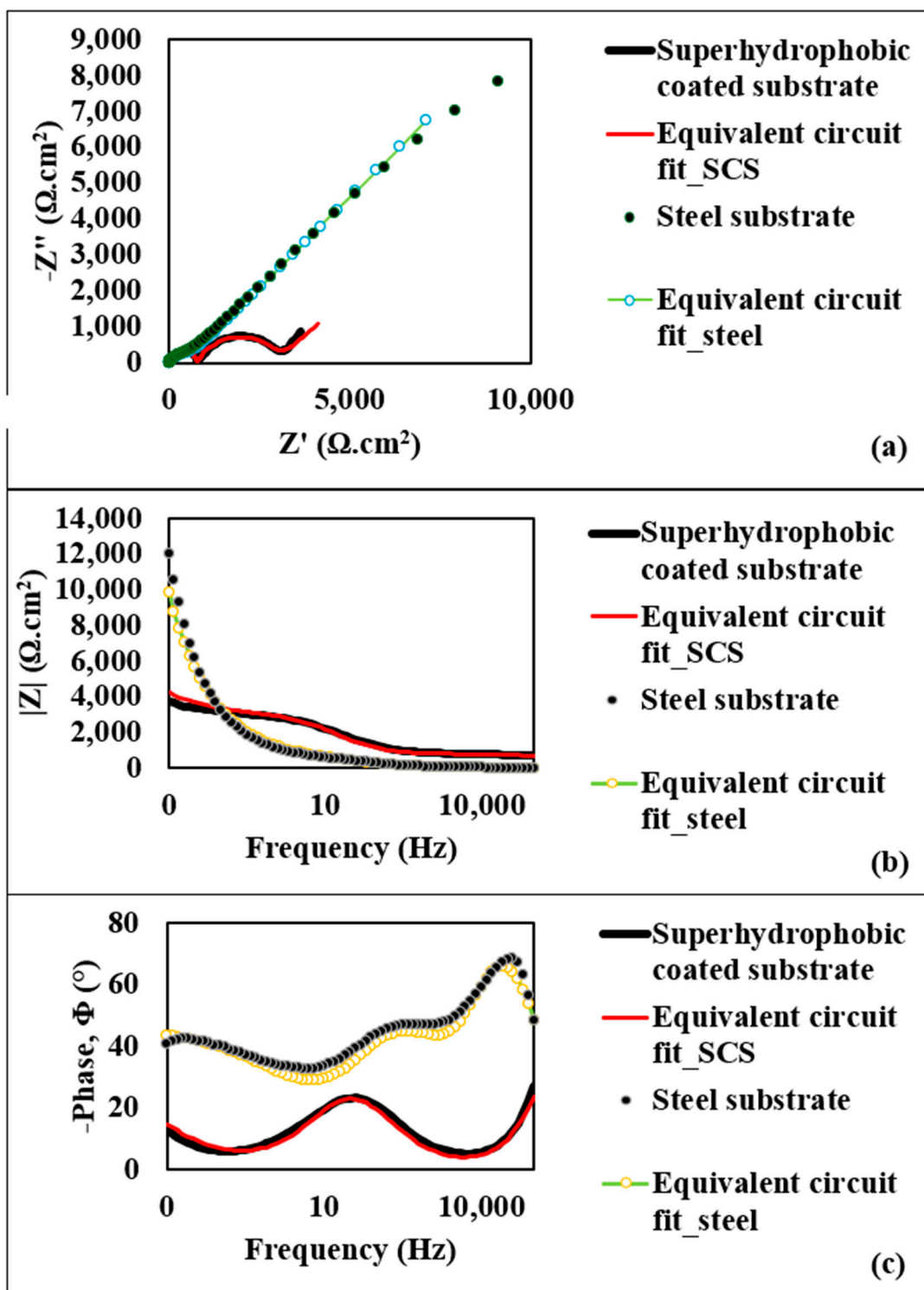
Figure 4. (**a**) Nyquist plot for steel substrate and the superhydrophobic coated substrate; (**b**) Bode modulus diagrams for steel substrate and the superhydrophobic coated substrate; (**c**) Bode phase angle diagrams for steel substrate and the superhydrophobic coated substrate.
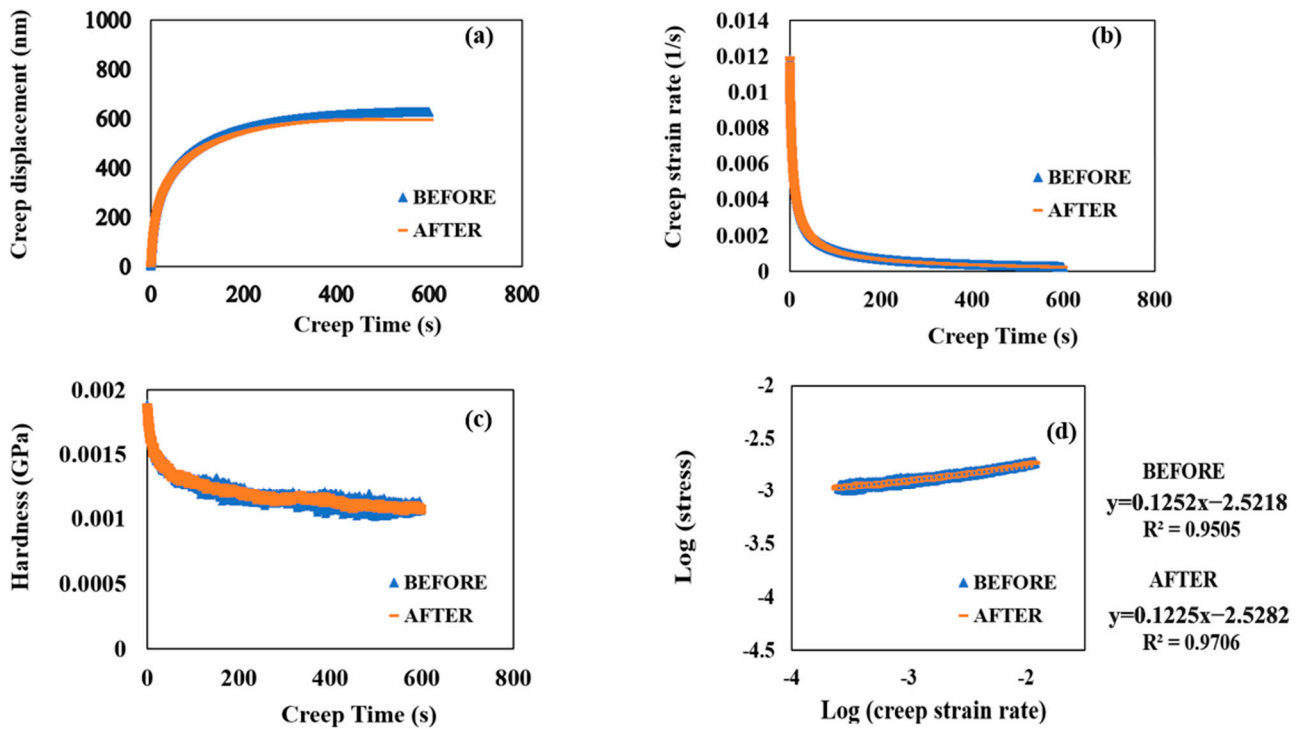
Figure 5. (**a**) Creep displacement versus creep time. (**b**) Creep strain rate versus creep time. (**c**) Hardness versus creep time. (**d**) Logarithmic stress versus logarithmic creep strain rate before and after 90 min of accelerated corrosion.

Figure 5b,c plot the values of creep strain rate and hardness against creep time, both before and after 90 min of accelerated corrosion. The creep strain rates significantly decreased from 0.01177 to 0.0019 s^{-1} during the first ~50 s. In comparison, the hardness values gradually decreased during the first ~50 s before declining linearly. As creep time increased, both hardness values continued to decrease. A logarithmic plot of the creep strain rate and stress yielded the creep strain rate sensitivity (m), a characteristic that indicates the stress response of samples to sudden changes in strain rate [24,30]:

$$\log(\text{stress}) = (1/m) \times \log(\text{strain rate}) + a1. \tag{2}$$

where a1 is the fitting coefficient

Notably, the strain rate sensitivity of SCS after 90 min of accelerated corrosion was evaluated as 0.122 from the creep tests under a load of 1000 μN (Figure 5d), which is very close to the pre-corrosion value of 0.125. This indicates that the m value of SCS is insensitive to corrosion. Additionally, during the creep tests, the logarithmic values of creep strain rate and stress exhibited a good linear relationship, increasing correspondingly from the lower left to the upper right corner (Figure 5d). Furthermore, no significant differences in creep resistance to indentation and comprehensive mechanical properties were observed after 90 min of accelerated corrosion.

To further characterize the viscoelasticity of the SCS sample, the nanoscale dynamic mechanical behavior of the material was investigated through nano-DMA. Figure 4 presents the hardness, storage modulus, loss modulus, and tan δ as functions of penetration depth.

Figure 6a,b show that both hardness and storage modulus exhibit a decreasing trend as penetration depth increases. The storage modulus, which represents the stiffness of the viscoelastic material and is proportional to the energy stored during deformation, initially decreases rapidly but then transitions to a slower, linear decrease. Importantly, there is no noticeable difference in the trends of hardness and storage modulus when

comparing the SCS sample before and after 90 min of accelerated corrosion, suggesting that the material retains its stiffness and resistance to deformation even after exposure to corrosive conditions.
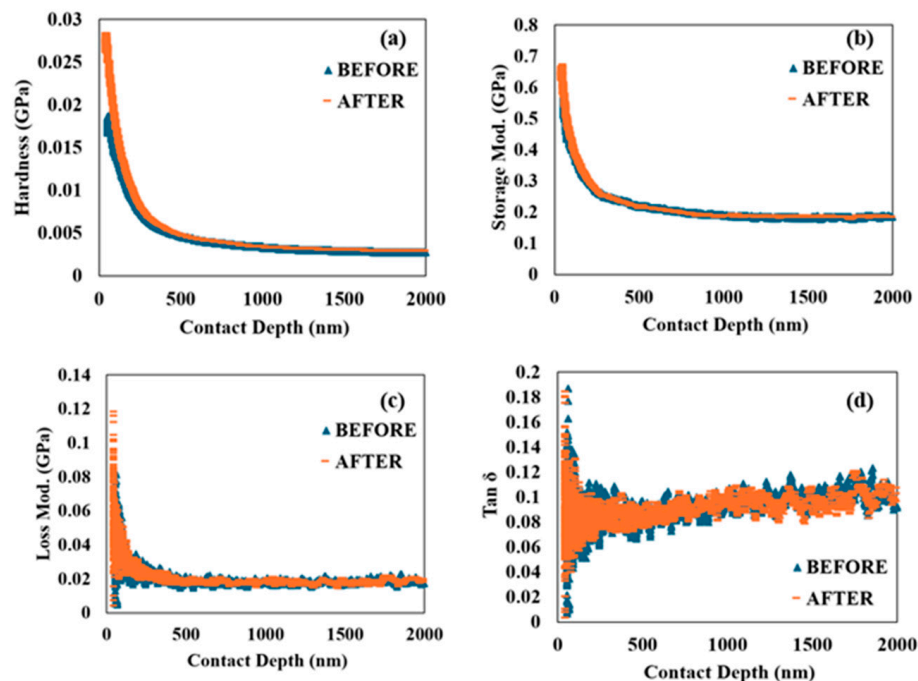

Figure 6. Nano dynamical mechanical analysis: (**a**) hardness versus contact depth; (**b**) storage modulus versus contact depth; (**c**) loss modulus versus contact depth; (**d**) tan δ versus contact depth before and after 90 min of accelerated corrosion.

Figure 6c,d provide a comparison of the loss modulus and tan δ, which are crucial indicators of the material's viscoelastic properties. The loss modulus initially shows a rapid increase. This behavior is indicative of the material's microstructural response to dynamic loading, where the initial response involves significant energy dissipation. Similarly, tan δ, the ratio of the loss modulus to the storage modulus, reflects the damping characteristics of the material. Both the loss modulus and tan δ decrease after the initial rise, eventually stabilizing at constant values.

The higher initial values of the loss modulus and tan δ suggest that the SCS sample's viscoelastic properties are significantly influenced by its nano/microstructures at the finest level. However, as penetration depth increases, these properties stabilize, indicating a consistent viscoelastic response beyond the top surface layer. Notably, the SCS sample shows no major differences in the loss modulus and tan δ before and after 90 min of accelerated corrosion. This implies that the material's ability to dissipate energy and its damping characteristics remain largely unaffected by the corrosive environment.

4. Conclusions

In this study, we characterized the corrosion resistance and mechanical and creep properties of superhydrophobic steel substrate at the nanoscale. Electrochemical impedance spectroscopy (EIS) results quantitatively confirm the enhanced anti-corrosion performance of the superhydrophobic coating. The nano-DMA results demonstrate that the superhydrophobic surface retains its viscoelastic properties, including hardness, storage modulus, loss modulus, and tan δ, even after exposure to accelerated corrosion. Based on the authors' understanding, this is the first time that these properties of a superhydrophobic surface have been reported at the nanoscale. The results also indicate the material's robustness under a corrosive condition, making it suitable for applications where both mechanical

integrity and resistance to environmental degradation are critical. The superhydrophobic coating has the potential to serve as an effective top coating, significantly enhancing the corrosion resistance of steel substrates.

References

1. Yang, W.; Li, J.; Zhou, P.; Zhu, L.; Tang, H. Superhydrophobic copper coating: Switchable wettability, on-demand oil-water separation, and antifouling. *Chem. Eng. J.* **2017**, *327*, 849–854. [CrossRef]
2. Wang, Z.; Li, Q.; She, Z.; Chen, F.; Li, L. Low-cost and large-scale fabrication method for an environmentally-friendly superhydrophobic coating on magnesium alloy. *J. Mater. Chem.* **2012**, *22*, 4097–4105. [CrossRef]
3. Jung, S.; Dorrestijn, M.; Raps, D.; Das, A.; Megaridis, C.M.; Poulikakos, D. Are superhydrophobic surfaces best for icephobicity? *Langmuir* **2011**, *27*, 3059–3066. [CrossRef]
4. Li, C.; Ma, R.; Du, A.; Fan, Y.; Zhao, X.; Cao, X. One-step fabrication of bionic superhydrophobic coating on galvanized steel with excellent corrosion resistance. *J. Alloys Compd.* **2019**, *786*, 272–283. [CrossRef]
5. Zhang, S.J.; Cao, D.L.; Xu, L.K.; Lin, Z.F.; Meng, R.Q. Fabrication of a superhydrophobic polypropylene coating on magnesium alloy with improved corrosion resistance. *Int. J. Electrochem. Sci.* **2020**, *15*, 177–187. [CrossRef]
6. Gong, A.; Zheng, Y.; Yang, Z.; Guo, X.; Gao, Y.; Li, X. Spray fabrication of superhydrophobic coating on aluminum alloy for corrosion mitigation. *Mater. Today Commun.* **2021**, *26*, 101828. [CrossRef]
7. Huang, J.; Lou, C.; Xu, D.; Lu, X.; Xin, Z.; Zhou, C. Cardanol-based polybenzoxazine superhydrophobic coating with improved corrosion resistance on mild steel. *Prog. Org. Coat.* **2019**, *136*, 105191. [CrossRef]
8. Yang, H.; Dong, Y.; Li, X.; Gao, Y.; He, W.; Liu, Y.; Mu, X.; Zhao, Y.; Fu, W.; Wang, X.; et al. Development of a mechanically robust superhydrophobic anti-corrosion coating using micro-hBN/nano-Al$_2$O$_3$ with multifunctional properties. *Ceram. Int.* **2025**, *51*, 491–505. [CrossRef]
9. She, Z.; Li, Q.; Wang, Z.; Li, L.; Chen, F.; Zhou, J. Novel method for controllable fabrication of a superhydrophobic CuO surface on AZ91D magnesium alloy. *ACS Appl. Mater. Interface* **2012**, *4*, 4348–4356. [CrossRef] [PubMed]
10. Zhu, X.; Zhang, Z.; Xu, X.; Men, X.; Yang, J.; Zhou, X.; Xue, Q. Facile fabrication of a superamphiphobic surface on the copper substrate. *J. Colloid Interface Sci.* **2012**, *367*, 443–449. [CrossRef] [PubMed]
11. Schaeffer, D.A.; Polizos, G.; Smith, D.B.; Lee, D.F.; Hunter, S.R.; Datskos, P.G. Optically transparent and environmentally durable superhydrophobic coating based on functionalized SiO$_2$ nanoparticles. *Nanotechnology* **2015**, *26*, 055602. [CrossRef] [PubMed]
12. Zhang, Z.; Ge, B.; Men, X.; Li, Y. Mechanically durable, superhydrophobic coatings prepared by dual-layer method for anticorrosion and self-cleaning. *Colloids Surf. A* **2016**, *490*, 182–188. [CrossRef]
13. Sebastian, D.; Yao, C.; Lian, I. Multiscale corrosion analysis of superhydrophobic coating on 2024 aluminum alloy in a 3.5 wt% NaCl solution. *MRS Commun.* **2020**, *10*, 305–311. [CrossRef]
14. Qing, Y.; Yang, C.; Hu, C.; Zheng, Y.; Liu, C. A facile method to prepare superhydrophobic fluorinated polysiloxane/ZnO nanocomposite coatings with corrosion resistance. *Appl. Surf. Sci.* **2015**, *326*, 48–54. [CrossRef]
15. Yu, J.; Qin, L.; Hao, Y.; Kuang, S.; Bai, X.; Chong, Y.M.; Zhang, W.; Wang, E. Vertically aligned boron nitride nanosheets: Chemical vapor synthesis, ultraviolet light emission, and superhydrophobicity. *ACS Nano* **2010**, *4*, 414–422. [CrossRef]
16. Boinovich, L.B.; Emelyanenko, A.M. The behaviour of fluoro-and hydrocarbon surfactants used for fabrication of superhydrophobic coatings at solid/water interface. *Colloids Surf. A* **2015**, *481*, 167–175. [CrossRef]
17. Tao, C.; Yan, H.; Yuan, X.; Yao, C.; Yin, Q.; Zhu, J.; Ni, W.; Yan, L.; Zhang, L. Synthesis of shape-controlled hollow silica nanostructures with a simple soft-templating method and their application as superhydrophobic antireflective coatings with ultralow refractive indices. *Colloids Surf. A* **2016**, *501*, 17–23. [CrossRef]

18. Wang, J.; Yang, C.; Liu, Y.; Li, Y.; Xiong, Y. Using Nanoindentation to Characterize the Mechanical and Creep Properties of Shale: Load and Loading Strain Rate Effects. *ACS Omega* **2022**, *7*, 14317–14331. [CrossRef]

19. Yang, C.; Liu, Y.; Wang, J.; Wu, D.; Liu, L.; Su, Z.; Xiong, Y. Application of nanoindentation technique in mechanical characterization of organic matter in shale: Attentive issues, test protocol, and technological prospect. *Gas Sci. Eng.* **2023**, *113*, 204966. [CrossRef]

20. Zhang, P.; Zhang, D.; Zhao, J. Control of fracture toughness of kerogen on artificially-matured shale samples: An energy-based nanoindentation analysis. *Gas Sci. Eng.* **2024**, *124*, 205266. [CrossRef]

21. Huang, H.; Zhang, W.; Shi, H.; Ni, J.; Ding, L.; Yang, B.; Zheng, Y.; Li, X. Experimental investigation of microscale mechanical alterations in shale induced by fracturing fluid contact. *Gas Sci. Eng.* **2024**, *124*, 205264. [CrossRef]

22. Wang, J.; Dziadkowiec, J.; Liu, Y.; Jiang, W.; Zheng, Y.; Xiong, Y.; Peng, P.A.; Renard, F. Combining atomic force microscopy and nanoindentation helps characterizing in-situ mechanical properties of organic matter in shale. *Int. J. Coal Geol.* **2024**, *281*, 104406. [CrossRef]

23. Sun, W.; Jiang, Y.; Zhang, Z.; Ma, Z.; Sun, G.; Hu, J.; Jiang, Z.; Zhang, X.; Ren, L. Nanoindentation creep behavior of nanocrystalline Ni and Ni-20 wt% Fe alloy and underlying mechanisms revealed by apparent activation volumes. *Mater. Des.* **2023**, *225*, 111479. [CrossRef]

24. Yan, C.; Bor, B.; Plunkett, A.; Domènech, B.; Maier-Kiener, V.; Giuntini, D. Nanoindentation creep of supercrystalline nanocomposites. *Mater. Des.* **2023**, *231*, 112000. [CrossRef]

25. Song, Y.; Ma, Y.; Pan, Z.; Li, Y.; Zhang, T.; Gao, Z. Nanoindentation Characterization of Creep-fatigue Interaction on Local Creep Behavior of P92 Steel Welded Joint. *Chin. J. Mech. Eng.* **2021**, *34*, 131. [CrossRef]

26. Ma, X.; Ma, J.; Bian, X.; Tong, X.; Han, D.; Jia, Y.; Wu, S.; Zhang, N.; Geng, C.; Li, P.; et al. The role of nano-scale elastic heterogeneity in mechanical and tribological behaviors of a Cu–Zr based metallic glass thin film. *Intermetallics* **2021**, *133*, 107159. [CrossRef]

27. Rath, A.; Mathesan, S.; Ghosh, P. Nanomechanical characterization and molecular mechanism study of nanoparticle reinforced and cross-linked chitosan biopolymer. *J. Mech. Behav. Biomed. Mater.* **2016**, *55*, 42–52. [CrossRef] [PubMed]

28. Díaz-Guillén, J.; Naeem, M.; Hdz-García, H.; Acevedo-Davila, J.; Díaz-Guillén, M.; Khan, M.; Iqbal, J.; Mtz-Enriquez, A. Duplex plasma treatment of AISI D2 tool steel by combining plasma nitriding (with and without white layer) and post-oxidation. *Surf. Coat. Technol.* **2020**, *385*, 125420. [CrossRef]

29. Hoque, M.A.; Yao, C.-W.; Lian, I.; Zhou, J.; Jao, M.; Huang, Y.-C. Enhancement of corrosion resistance of a hot-dip galvanized steel by superhydrophobic top coating. *MRS Commun.* **2022**, *12*, 415–421. [CrossRef]

30. Holz, H.; Merle, B. Novel nanoindentation strain rate sweep method for continuously investigating the strain rate sensitivity of materials at the nanoscale. *Mater. Des.* **2023**, *236*, 11247. [CrossRef]